INTERNATIONAL JOURNAL FOR NUMERICAL METHODS IN FLUIDS
Int. J. Numer. Meth. Fluids 2006; **50**:885–909
Published online 17 October 2005 in Wiley InterScience (www.interscience.wiley.com). DOI: 10.1002/fld.1083

Solid-particle erosion in the tube end of the tube sheet of a shell-and-tube heat exchanger

M. A. Habib[1,*,†], H. M. Badr[1], S. A. M. Said[1], R. Ben-Mansour[1] and S. S. Al-Anizi[2]

[1]*Mechanical Engineering Department, King Fahd University of Petroleum and Minerals, Dhahran 31261, Saudi Arabia*
[2]*Saudi ARAMCO, Saudi Arabia*

SUMMARY

Erosion is one of the major problems in many industrial processes, and in particular, in heat exchangers. The effects of flow velocity and sand particle size on the rate of erosion in a typical shell-and-tube heat exchanger were investigated numerically using the Lagrangian particle-tracking method. Erosion and penetration rates were obtained for sand particles of diameters ranging from 10 to 500 μm and for inlet flow velocities ranging from 0.197 to 2.95 m/s. A flow visualization experiment was conducted with the objective of verifying the accuracy of the continuous phase calculation procedure. Comparison with available experimental data of penetration rates was also conducted. These comparisons resulted in a good agreement. The results show that the location and number of eroded tubes depend mainly on the particle size and velocity magnitude at the header inlet. The rate of erosion depends exponentially on the velocity. The particle size shows negligible effect on the erosion rate at high velocity values and the large-size particles show less erosion rates compared to the small-size particles at low values of inlet flow velocities. The results indicated that the erosion and penetration rates are insignificant at the lower end of the velocity range. However, these rates were found to increase continuously with the increase of the inlet flow velocity for all particle sizes. The particle size creating the highest erosion rate was found to depend on the flow velocity range. Copyright © 2005 John Wiley & Sons, Ltd.

KEY WORDS: solid-particle erosion; heat exchanger; tube sheet; shell-and-tube

1. INTRODUCTION

Erosion is defined as the loss of material due to repeated application of mechanical forces resulting from the impingement of solid particles on a surface. Erosion is one of the major

*Correspondence to: M. A. Habib, Mechanical Engineering Department, King Fahd University of Petroleum and Minerals, P.O. Box 1866, Dhahran 31261, Saudi Arabia.
†E-mail: mahabib@kfupm.edu.sa

Contract/grant sponsor: King Fahd University of Petroleum and Minerals
Contract/grant sponsor: Saudi Aramco

Received 30 January 2005
Revised 1 August 2005
Accepted 11 August 2005

problems in many industrial processes, and in particular, in heat exchangers utilizing seawater for cooling purposes and oil and gas production facilities. It results in severe damage of different flow passages causing frequent failure of various equipments and leading to higher cost of maintenance as well as the loss of valuable production time. The erosion mechanism can occur in the form of direct impingement erosion when the particles have significant momentum towards the walls such as heat exchanger tubes in shell and tube heat exchangers. It can also occur in straight sections as a result of turbulent fluctuations that create a mechanism known as random impingement.

The problem of erosion in heat exchanger tubes does not only affect the reliability and overall performance of heat exchangers but also increases significantly the cost of operation. The previous work done on erosion in straight tubes, elbows and tees show the strong influence of fluid properties, sand size and flow velocity on the rate of erosion [1–7]. The recent experimental study [8] on erosion in elbows and straight pipes provided correlations between the penetration rate and the velocity at different elbow diameters and sand rate and size. Edwards *et al.* [9] reported the effect of the bend angle on the normalized penetration rate. The objective of most of these experimental studies was to provide data for establishing a relationship between the amount of erosion and the physical characteristics of the materials involved, as well as the particle velocity and impact angle.

One of the difficult problems faced in predicting the rate of erosion numerically is the determination of the particle impact velocity, impingement angle and the frequency of surface impacts. The numerical approach to erosion modelling constitutes a combination of flow modelling, Lagrangian particle tracking, and the use of erosion equations. This model, which is sometimes called the Lagrangian approach, requires expertise in fluid dynamic modelling and a large amount of computational work. In this approach, it is assumed that the particles are not interacting within the flow field. The conditions for this phenomenon correspond to fairly dilute systems characterized by volume fractions (volume of solids/total volume) of less than 10^{-3}. While a Lagrangian description of particle motion implies a discrete particle phase, an Eulerian description treats the particle phase as a continuum that permits appropriate definitions of averaged fluid quantities. Many authors [10–12] carried out comparisons between the Lagrangian and Eulerian approaches. The utilization of computational fluid dynamics (CFD) for obtaining the flow field characteristics together with modelling particle trajectories using Lagrangian simulation of particle motion can predict erosive wear in a complex geometry such as that of multi-orifice choke valves [13].

Graham [14] summarized the approaches used for developing Lagrangian models in the research conducted prior to 1996. Wang *et al.* [15] developed a computational model for predicting the rate of erosive wear in a 90° elbow. The flow field was first obtained through a computational model in which the governing equations of motion were solved numerically, thereby neglecting the presence of the solid particles (single-phase flow). The particle trajectory and impacting velocity were then determined by solving the equation of particle motion taking into consideration drag, buoyancy and virtual mass effects. The penetration rate was then obtained using a semi-empirical relation that was previously developed [16]. A comparison between the predicted penetration rates and the available experimental data showed a good agreement.

McLaury *et al.* [8] extended the mechanistic model that was developed earlier for predicting erosion in standard elbows [17, 18] to predict erosion in long-radius elbows. In that work, they accounted for the elbow radius of curvature and for the effect of turbulent fluctuations of the

flow. Their results agreed well with the experimental data and the results obtained using a general model consisting of a flow model, a particle-tracking model, and an erosion model. They also developed a mechanistic model for predicting erosion in straight pipes. In that model, random impingements were employed in the erosion mechanism to predict penetration rates. The prediction of penetration rates in long radius elbows and in straight pipes was carried out using semi-empirical correlations. The results for air and water showed a good agreement with those obtained using a general model. More recently, other Lagrangian models involving the use of CFD packages were developed, as for example, the use of PHOENICS [19, 20]. In addition, the CFX code was used [21] for predicting erosion within oilfield control valves and the CFD code was used [9] to predict erosion in a pipe bend fitting made of carbon steel.

Although the tube entrance region in heat exchangers is the most critical with respect to erosion, there is no research published in the literature that deals with the effect of various parameters on erosion in that region. The present research work aims at studying the effect of different fluid flow parameters on the rate of erosion at the entrance region of heat exchanger tubes under conditions simulating the normal working conditions of a typical shell and tube heat exchanger. The calculations of flow patterns and solid particle trajectories inside the inlet header of the heat exchanger were performed and the correlations available in the literature were used for estimating the rate of erosion.

2. THE FLOW DOMAIN AND THE GOVERNING PARAMETERS

The calculations were performed inside the inlet header of the heat exchanger and the tubes of the tube sheet. Figure 1 shows the geometry of the header. Flow enters the nozzle of the heat exchanger header. Abrupt expansion occurs at connection with the header. Water then flows towards the tube sheet, Figure 2. The tube sheet has 38 tubes of diameter 19.8 mm distributed in half a circle as shown in the figure. Due to symmetry, only half of the tubes were considered. Uniform inlet flow velocity was considered. The flow velocity ranged from 0.197 to 2.95 m/s. Sand particles of density 2650 kg/m^3 having diameter in the range of 10–500 μm were considered.

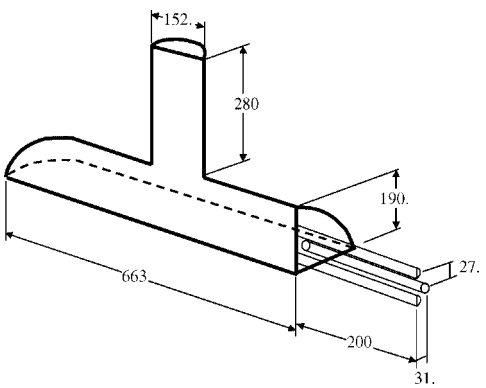

Figure 1. The main dimensions of the computational domain of the shell-and-tube heat exchanger (all dimensions in mm).

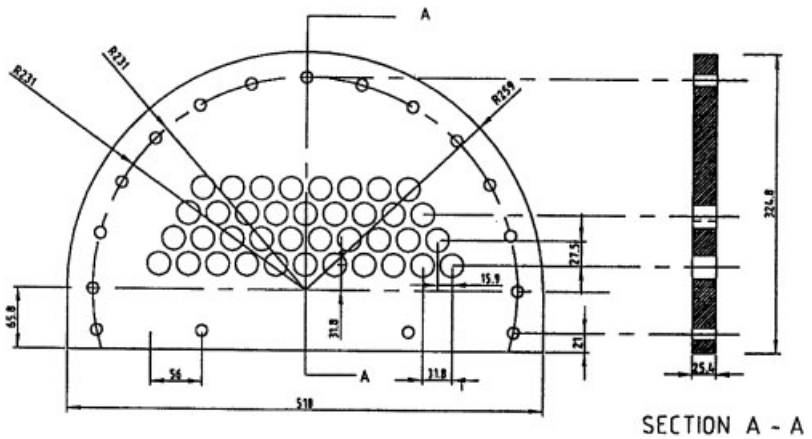

Figure 2. The tube sheet showing the arrangement of heat exchanger tubes.

3. THE CALCULATION PROCEDURE

It has been established that the rate of erosion in tubes depends upon many parameters such as the properties of the impacting particles, the properties of the tube material, and the other parameters of the impact process [22–24]. Thus, the flow field characteristics and the details of the particle impact process as well as the erosion rate correlations are required for the prediction of the rate of erosion in tubes. In the present work, the Lagrangian particle tracking method is used to model the erosion process. The Lagrangian particle tracking method represents a one-way flow-to-particle coupling method that can be used when low volume of particles is simulated. Two computational models were developed. The first is the continuous phase model (dealing with the prediction of the flow velocity field) and the second is the particle-tracking model (dealing with the prediction of particle motion). A brief discussion of the two models is presented in the following sections.

3.1. The continuous phase model

To predict the flow pattern of the continuous flow phase, the conservation equations for mass and momentum are solved. Additional transport equations for the turbulence model are also solved since the flow is turbulent. The time-averaged governing equations of 3-D turbulent flow can be found in many references [25, 26] and can be presented as follows.

3.1.1. The continuity and momentum equations

Mass conservation: The steady state time-averaged equation for conservation of mass can be written as

$$\frac{\partial}{\partial x_j}(\rho \bar{U}_j) = 0 \tag{1}$$

Momentum conservation: The steady-state time-averaged equation for the conservation of momentum in the i direction can be expressed as

$$\frac{\partial}{\partial x_j}(\rho \bar{U}_i \bar{U}_j) + \frac{\partial}{\partial x_j}(\rho \overline{u_i u_j}) = -\frac{\partial p}{\partial x_i} + \frac{\partial}{\partial x_j}\left(\mu \frac{\partial U_i}{\partial x_j}\right) \tag{2}$$

where p is the static pressure. The stress tensor $\rho \overline{u_i u_j}$ is given by

$$-\rho \overline{u_i u_j} = \left[\mu_{\text{eff}}\left(\frac{\partial \bar{U}_i}{\partial x_j} + \frac{\partial \bar{U}_j}{\partial x_j}\right)\right] - \frac{2}{3}\rho k \delta_{ij} \tag{3}$$

where δ_{ij} is the Kronecker delta which is equal to 1 for $i = j$ and equals 0 for $i \neq j$ and $\mu_{\text{eff}} = \mu_t + \mu$ is the effective viscosity. The turbulent viscosity, μ_t, is calculated using the high-Reynolds number form as

$$\mu_t = \rho C_\mu \frac{k^2}{\varepsilon} \tag{4}$$

with $C_\mu = 0.0845$. The value of C_μ is derived using the mathematical model RNG 'renormalization group' [27] to accurately describe the variation of turbulent transport with effective Reynolds number, thus, providing better results for near wall flows. The value of C_μ used in the present study is therefore different from the value 0.09 used for high Reynolds number. k and ε are the kinetic energy of turbulence and its dissipation rate. These are obtained by solving their conservation equations as given below.

3.1.2. Conservation equations for the turbulence model. The conservation equations of the turbulence model [28, 29] are given as follows:

The kinetic energy of turbulence:

$$\frac{\partial}{\partial x_j}(\rho \bar{U}_j k) = \frac{\partial}{\partial x_j}\left(\frac{\mu_{\text{eff}}}{\sigma_k}\frac{\partial k}{\partial x_i}\right) + G_k - \rho\varepsilon \tag{5}$$

The rate of dissipation of the kinetic energy of turbulence:

$$\frac{\partial}{\partial x_j}(\rho \bar{U}_j \varepsilon) = \frac{\partial}{\partial x_i}\left(\frac{\mu_{\text{eff}}}{\sigma_\varepsilon}\frac{\partial \varepsilon}{\partial x_i}\right) + C_{\varepsilon 1} G_k \frac{\varepsilon}{k} - C_{\varepsilon 3}\rho \frac{\varepsilon^2}{k} \tag{6}$$

where G_k represents the generation of turbulent kinetic energy due to the mean velocity gradients and is given by

$$G_k = -\rho \overline{u_i u_j}\frac{\partial \bar{U}_j}{\partial x_i} \tag{7}$$

The quantities σ_k and σ_ε are the effective Prandtl numbers for k and ε, respectively, and $C_{\varepsilon 3}$ is given [29] as a function of the term k/ε and, therefore, the model is responsive to the effects of rapid strain and streamline curvature and is suitable for the present calculations. Thus, $C_{\varepsilon 3}$ is expressed as

$$C_{\varepsilon 3} = C_{\varepsilon 2} + \frac{C_\mu \rho \eta^3 (1-\eta)/\eta_o}{1 + \beta\eta^3}$$

with $\eta = Sk/\varepsilon, \eta_o = 4.38, \beta = 0.012$. S being a scalar measure of the deformation tensor given by $S = \sqrt{2\omega_{ij}\omega_{ij}}$ where

$$\omega_{ij} = 0.5\left(\frac{\partial u_j}{\partial x_i} - \frac{\partial u_i}{\partial x_j}\right)$$

The model constants $C_{\varepsilon 1}$ and $C_{\varepsilon 2}$ have the values; $C_{\varepsilon 1} = 1.42$ and $C_{\varepsilon 2} = 1.68$.

The wall functions establish the link between the field variables at the near-wall cells and the corresponding quantities at the wall. These are based on the assumptions introduced [30] and have been most widely used for industrial flow modelling. Sensitivity analysis was performed using different wall treatments including standard wall function, non-equilibrium wall functions employing the two layer concept and the near wall treatment model. It is found that the influence of wall parameters on the velocity magnitude (particularly at the high values of the velocity) and consequently on the erosion rates is insignificant.

3.1.3. Boundary conditions. The velocity distribution is considered uniform at the header inlet section with the velocity in the direction of the nozzle axis. Kinetic energy and its dissipation rate are assigned through a specified value of $\sqrt{k/\bar{U}^2}$ equal to 0.1 and a length scale, L, equal to the diameter of the header inlet nozzle. The boundary condition applied at the exit section (outlet of the heat exchanger tubes) is that of fully developed flow. At the wall boundaries, all velocity components are set to zero in accordance with the no-slip and impermeability conditions. Kinetic energy of turbulence and its dissipation rate are determined from the equations of the turbulence model.

3.1.4. Solution procedure. The conservation equations are integrated and solved simultaneously over a typical volume that is formed by division of the flow field into a number of control volumes, to yield the solution. Calculations are performed with at least 200 000 elements considering fine elements in the section of the header close to the inlet to heat exchanger tubes. Convergence is considered when the maximum of the summation of the residuals of all the elements for U, V, W and pressure correction equations is less than 0.1%. Due to the complexity of the problem, a hybrid (upwind central differencing) scheme was used rather than a higher order scheme. The grid independence tests were performed by increasing the number of control volumes from 200 000 to 418 000 in two steps; 200 000–301 000 and 301 000–418 000. The velocity magnitudes of the different cases of mesh sizes were compared at the symmetry plane and close to the inlet to the heat exchanger tubes. The influence of refining the grid on the continuous-phase velocity field is less than 1.5% and indicates that more mesh refinement will result in negligible changes in the results of the computational model. It should be noted here that the erosion rate depends fully on the velocity magnitude and angle. Therefore, the accurate prediction of velocity results in accurate prediction of erosion rates.

3.2. Particle tracking

The particle impact velocity is obtained by determining the particle trajectory from the moment it enters the inlet header until it leaves the heat exchanger tubes. One of the main assumptions in this study is that the solid particles are not interacting with each other. Moreover, the influence of particle motion on the fluid flow field is considered very small and

can be neglected. These two assumptions are based on the condition of fairly dilute particle concentration. The same assumptions were made [9, 13, 18, 19, 31, 32] in the solution of similar problems of low particle concentration (less than 2–3% by weight). It is also assumed that the influence of continuous phase turbulence on particle impact velocity and angle close to the wall is neglected in comparison to the mean flow effect. This assumption was considered by many other investigators [9, 15, 20, 21]. This assumption is justified by analysing the experimental results [33] where random erosion downstream of sudden expansion does not exceed 2.5% as compared to impingement erosion. This justifies neglecting the influence of the continuous phase turbulence on particle impact velocity and angle compared to the mean flow influence.

Taking the main hydrodynamic forces into consideration, the particle equation of motion can be written as

$$\frac{\mathrm{d}\underline{u}_\mathrm{p}}{\mathrm{d}t} = F_\mathrm{D}(\underline{u} - \underline{u}_\mathrm{p}) + \underline{g}(\rho_\mathrm{p} - \rho)/\rho_\mathrm{p} + \underline{F}_\mathrm{vm} + \underline{F}_\mathrm{pg} + \underline{F}_\mathrm{sl} \tag{8}$$

where $F_\mathrm{D}(\underline{u} - \underline{u}_\mathrm{p})$ is the drag force per unit particle mass and $F_\mathrm{D} = 3C_\mathrm{D}\mu Re_\mathrm{p}/4\rho_\mathrm{p}D_\mathrm{p}^2$, $\underline{g}(\rho_\mathrm{p} - \rho)/\rho_\mathrm{p}$ is the buoyancy force term, $\underline{F}_\mathrm{vm}$ is the virtual mass term (force required to accelerate the fluid surrounding the particle), $\underline{F}_\mathrm{pg}$ is the pressure gradient term and $\underline{F}_\mathrm{sl}$ is the Saffman lift force [34]. The Magnus lift force (resulting from particle rotation) and the Basset history force (the force accounting for the flow field unsteadiness) have been neglected. The particle Reynolds number, Re_p, and the drag coefficient, C_D, are obtained from

$$Re_\mathrm{p} = \frac{\rho D_\mathrm{p}|\underline{u}_\mathrm{p} - \underline{u}|}{\mu} \tag{9}$$

$$C_\mathrm{D} = a_1 + \frac{a_2}{Re_\mathrm{p}} + \frac{a_3}{Re_\mathrm{p}^2} \tag{10}$$

where the a_1, a_2 and a_3 are constants given [35] for smooth spherical particles over several ranges of Re. Another equation that is frequently used for C_D [36] is given by

$$C_\mathrm{D} = \frac{24}{Re_\mathrm{p}}(1 + b_1 Re_\mathrm{p}^{b_2}) + \frac{b_3 Re_\mathrm{p}}{b_4 + Re_\mathrm{p}} \tag{11}$$

where b_1, b_2, b_3 and b_4 are expressed in terms of the surface area of a sphere having the same volume as the particle to the actual surface area of the particle.

In the present case of low particle concentration, the particles motions are considered non-interacting and the dominant forces in Equation (8) are the drag force [9], the buoyancy force and the virtual mass force. Other forces given in Equation (8) are of small order of magnitude and are neglected in this study. The first of these is the virtual mass term that takes care of the force required to accelerate the fluid surrounding the particle. This term can be expressed as

$$\underline{F}_\mathrm{vm} = \frac{1}{2}\frac{\rho}{\rho_\mathrm{p}}\frac{\mathrm{d}}{\mathrm{d}t}(\underline{u} - \underline{u}_\mathrm{p}) \tag{12}$$

and is important when the fluid density and particle density are similar. In this study, the virtual mass force is considered.

3.2.1. Integration of the particle trajectory equations. The particle trajectory equations are solved by stepwise integration over discrete time steps. Integration in time of the equation of particle motion yields the velocity of the particle at each point along the trajectory, with the trajectory itself predicted by

$$\frac{\mathrm{d}\underline{r}}{\mathrm{d}t} = \underline{u}_{\mathrm{p}} \tag{13}$$

where $\underline{r}$ is the position vector. The above equation is integrated in each coordinate direction to predict the trajectories of the discrete phase.

3.2.2. Discrete phase boundary conditions. The boundary conditions considered when a particle strikes a boundary surface depends on the nature of that surface. When reflection via an elastic or inelastic collision occurs, the normal coefficient of restitution which defines the amount of momentum in the direction normal to the wall that is retained by the particle after colliding with the boundary [37] is taken as 0.9 in the present calculations for the cases of reflection at a wall. The calculations of the particle trajectory are terminated at the point when it passes through an open boundary (the exit section of any of the heat exchanger tubes). When the particle encounters such boundary, it is considered that the particle has escaped and the trajectory calculations are then terminated. The trajectory calculations for some particles (normally very few particles) are terminated when the particles get trapped in the flow field. This is found to occur when a particle circulates in a confined flow zone. In such a case, the trajectory calculations are terminated.

3.3. The erosion model

The previous experimental results [24, 38] show that the erosive wear-rate exhibits power-law velocity dependence. The velocity exponent ranges from 1.9 to 2.5. The results also indicate that the erosion rate is a function of the angle of impact. Prediction of erosion in straight pipes, elbows and tees show the strong influence of fluid properties, sand size and flow velocity on the rate of erosion [17, 18, 33, 39]. There have been many attempts in the past to represent the solid particle erosion process by an analytical formula that could be used to predict erosion under any condition. The complexity of the erosion process and the number of factors involved has meant that no generally applicable equation has been forthcoming. Almost all of the formulae generated have therefore some degree of dependence on empirical coefficients provided by various experimental erosion tests. No definitive theory of erosion currently exists, however, a number of qualitative and quantitative models do exist. These are described in References [9, 19, 40–42].

The empirical erosion equations suggested [43] were used [13] to correlate the experimental erosion data to provide an erosion modelling technique. Wallace *et al.* [13] provided the following formula that proved to provide good results as compared to the experimental data:

$$E = \frac{1}{N_{\mathrm{p}}} \left\{ \frac{\frac{1}{2}u_{\mathrm{p}}^2 \cos^2 \alpha \sin 2\alpha}{\gamma} + \frac{\frac{1}{2}u_{\mathrm{p}}^2 \sin^2 \alpha}{\sigma} \right\} \alpha \leqslant 45 \tag{14}$$

$$E = \frac{1}{N_{\mathrm{p}}} \left\{ \frac{\frac{1}{2}u_{\mathrm{p}}^2 \cos^2 \alpha}{\gamma} + \frac{\frac{1}{2}u_{\mathrm{p}}^2 \sin^2 \alpha}{\sigma} \right\} \alpha > 45^\circ \tag{15}$$

γ and σ are the cutting wear and deformation wear coefficients $\gamma = 33\,316.9, \sigma = 77\,419.7$ for low velocity [13]. This formula is valid for target material of carbon steel and is used in the present calculations of the erosion rate.

Through the tracking model, impingement information is gathered as particles impinge the walls of the geometry. As particle trajectories are computed, this impingement information is recorded and erosion is computed using empirical relations. Knowledge of the particle impact speed and impact angle allows the erosion rate to be computed. The calculations of the continuous phase and the particle tracking were obtained using the Fluent CFD-5.5 package [44]. The ability to predict erosion was provided by the authors through FORTRAN subroutines that are used along with the CFD code.

3.4. The penetration model

The local penetration rate is one of the important erosion parameters since it represents the depth of wear at various locations on the solid surface. In this work, the inner volume of the inlet header was discretized using a large number of finite volumes (cells). The mass loss for all solid particle impingements was compiled to generate the local penetration rate for each boundary cell. At any given boundary cell, the local penetration rate, P_n, was calculated using the following equation [15, 17]:

$$P_n = 31.536 \times 10^6 \frac{\dot{s}}{\rho_{\mathrm{m}} A} E_{\mathrm{lc}} \tag{16}$$

where A is the impingement area (m^2), E_{lc} is the local erosion rate (mg/g), P_n is the penetration rate (mm/year), $\dot{s}$ is the sand rate (kg/s) and ρ_{m} is the density of target material ($\mathrm{kg/m}^3$). The results obtained for erosion and penetration rates in the header of a shell-and-tube heat exchanger are presented in the following sections.

4. FLOW VISUALIZATION EXPERIMENTS

Flow visualization experiments were conducted to validate the numerical scheme used for modelling the continuous phase flow field for the shell-and-tube heat exchanger. The flow field in the heat exchanger inlet header was visualized by injecting fine solid particles that were illuminated using a two-dimensional laser light sheet. The particle trajectory traces were photographed using a high-speed digital camera. The experimental setup is composed of two main parts, namely, the flow loop and the test section. Figure 3 shows a schematic of the flow loop together with the names of various components. As can be seen in Figure 3, the flow loop is a closed-type loop that consists of a pump, a piping system and two reservoirs. The lower reservoir is made of fibreglass and has a total volume of $1\ \mathrm{m}^3$. The upper reservoir is used as a settling chamber that is utilized to minimize the lateral flow fluctuations and unsteady flow oscillations in order to provide a steady uniform flow at the inlet of the header nozzle. The piping system is made of 2-inch PVC pipes and is equipped with three valves. The two gate valves are used as suction and delivery valves installed immediately before and after the pump and the ball valve is installed downstream of the heat exchanger. Water is pumped from the lower reservoir to the settling chamber and back to the lower reservoir through the

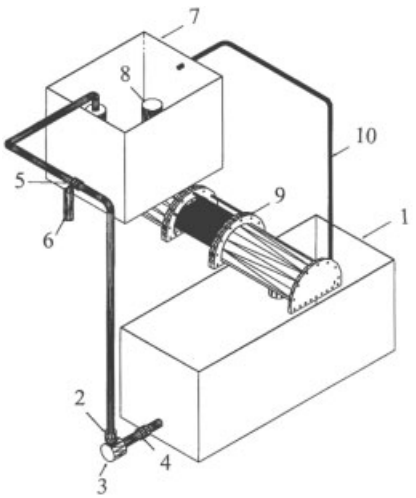

Schematic of the Test Rig

1. Water Reservoir
2. Valve
3. Water Pump
4. Valve
5. Orifice Meter
6. U-Tube
7. Settling Chamber
8. Inlet Nozzle
9. Test Section
10. Overflow Pipe

Figure 3. The flow visualization experimental setup: schematic of the flow loop.

test section. The pump delivery valve together with the ball valve (installed downstream of the test section) are used to control the volume flow rate in the test section.

5. RESULTS AND DISCUSSION

5.1. Validation

Figure 4(a) shows the visualized flow pattern in a transverse vertical section of the inlet header parallel to the tube sheet, and located at the middle section of the inlet pipe. The flow pattern shows a jet-like flow issuing from the inlet pipe and impacting the header base plate creating a three-dimensional stagnation flow zone that resembles Hiemens flow [45]. Due to the curved (cylindrical) walls of the inlet header, two counter-rotating vortices appeared on both sides of the jet. The exact size and shape of these vortices depend on the inlet flow velocity as well as the shape and size of the inlet header. The flow velocity vectors at the same section were predicted using the continuous phase model. The model prediction was performed to simulate the same experimental conditions. These conditions included the same inlet flow velocity ($V_i = 0.3$ m/s) and the same fluid properties. Figure 4(b) shows the computational prediction of the flow pattern which is close to the visualized pattern shown in Figure 4(a). It is worth mentioning that the computational prediction shows the velocity vectors at various points of the flow field while the visualized pattern shows traces of the small wooden particles. Moreover, the computational prediction shows the mean velocity vectors at various points of the chosen section since the governing equations are of time-averaged Eulerian type. As can be seen in Figures 4(a) and (b), the predicted flow patterns are in good agreement with the visualized ones indicating the accuracy of the computational model.

To verify the accuracy of the computational scheme, calculations of the erosion rate for pipe contraction were performed and the results were compared with the experimental data of

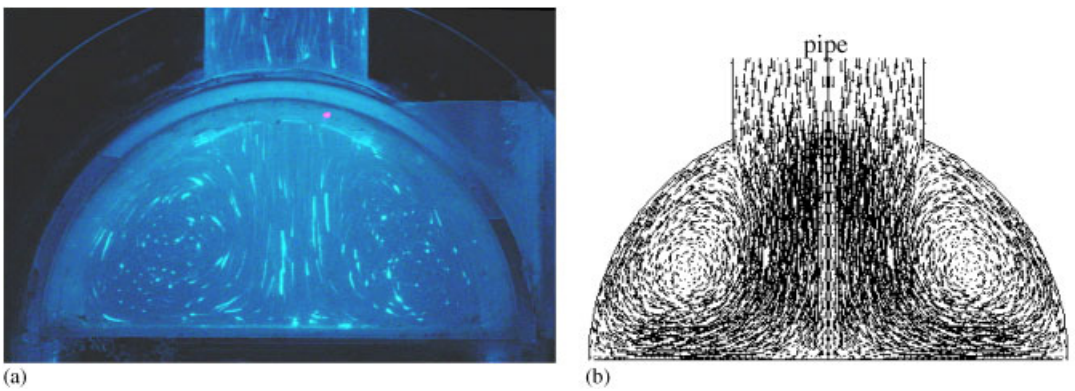

Figure 4. Comparison between the visualized flow pattern and the computed velocity vectors at a transverse vertical section of the inlet header: (a) visualized traces of particle trajectories photographed at the middle section of the inlet pipe; and (b) the computed velocity vectors.

Postlethwaite and Nesic [33]. The pipe sudden contraction simulates the tube sheet in the heat exchanger. The experimental data were obtained for a pipe contraction ratio of $d/D = 0.5$. The large tube has a 42.1 mm diameter and an inlet velocity of 3.3 m/s. Three values of particle concentration of 2, 5 and 10%, by volume, were considered. The sand particle diameter was 430 μm. Short 3-mm segments were used at the inlet region of the sudden contraction to determine the penetration rate. In the present calculations, the step height was divided to 1000 discs, then, data were integrated to give the results over a disc of 3 mm width having its inner diameter as the smaller tube. Stochastic tracking was utilized and a total of 30 trials, each injected at a random basis, was conducted. The results were averaged to obtain the particle impact velocity and angle. The results of the comparison are given in Figure 5 in terms of the penetration rate. The comparison shown in Figure 5 indicates a reasonably good agreement. Validation was also conducted against the results of Blatt *et al.* [46] for sudden contraction of 0.5 diameter ratio. The particle volume percent was 0.1%. Comparison was made at different velocity values as shown in Figure 6 and again shows good agreement.

5.2. The flow velocity field

The continuous-phase model was applied to predict the details of the flow velocity field inside the inlet header of the shell-and-tube heat exchanger using water as the fluid medium. The lengths of the heat exchanger tubes downstream of the header are shorter than those in the prototype but long enough to achieve fully developed turbulent flow. This was mainly done to reduce the size of the computational domain without affecting the accuracy of the computed flow velocity field. The flow velocity at the header inlet nozzle, V_i, ranged from 0.197 to 2.95 m/s with the intermediate values of 0.3, 0.64 and 1.31 m/s. It is worth mentioning that the typical velocity for the considered heat exchanger operating condition is 0.64 m/s. The lower and upper bounds of the considered velocity range correspond to the limits of serious fouling and erosion conditions [47]. Because of the header geometry and the considered range of inlet velocity, the resulting flow is turbulent and three-dimensional. To provide some details of the flow velocity field, the velocity contours (coloured by velocity magnitude) at the plane

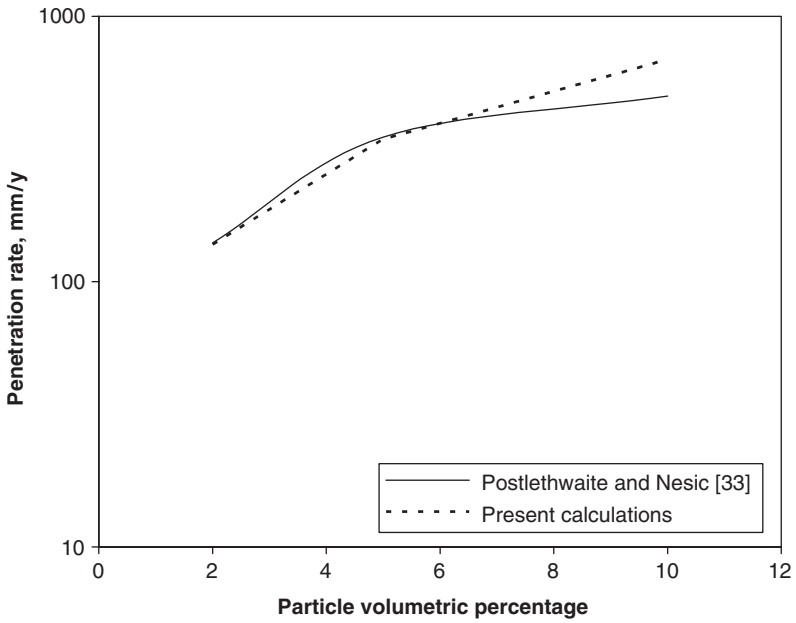

Figure 5. Comparison of the calculated penetration rate and the experimental data of Postlethwaite and Nesic [33].

of symmetry are plotted in Figure 7(a) for the case of $V_i = 0.64$ m/s. The figure indicates almost uniform velocity distribution in the inlet pipe, low velocities (less than 0.2 m/s) near the upper wall of the header and reaching about 0.4 m/s in the core region. As the water jet impinges the header bottom, it is partially diverted towards the tube sheet and partially towards the circulating flow zone at the opposite side of the tube sheet. The figure shows two large vortices of opposite direction at the boundaries of the inlet flow jet. These are created by the entrained flow in the low velocity regions at the two opposite sides of the jet. The flow near the tube sheet becomes streamlined to enter the different tubes. A close view of the velocity contours upstream and downstream of the tube entrance section is shown in Figure 7(b). The figure clearly shows that the fluid velocity accelerates upstream of the tube inlet section and that acceleration continues until reaching the maximum velocity at a distance of approximately one tube diameter downstream of the tube inlet section.

Although the prevailing flow velocity in the header is much less than V_i, the velocity in the immediate neighbourhood of the tube sheet (towards the tube inlet section) is higher than V_i and becomes much higher downstream of the tube inlet section (the *vena contracta* effect). The figure also shows two regions of low velocity located at the top and bottom corners of the header close to the tube sheet. The directions and magnitudes of the velocity vectors at the tube inlet section are dependent on the tube position. For the sake of presenting the three-dimensional character of the flow field inside the inlet header, the pathlines (stream traces) of a limited number of fluid particles are plotted in Figure 8 for the same case of $V_i = 0.64$ m/s. Because of symmetry, the pathlines are only plotted in one half of the header. The figure

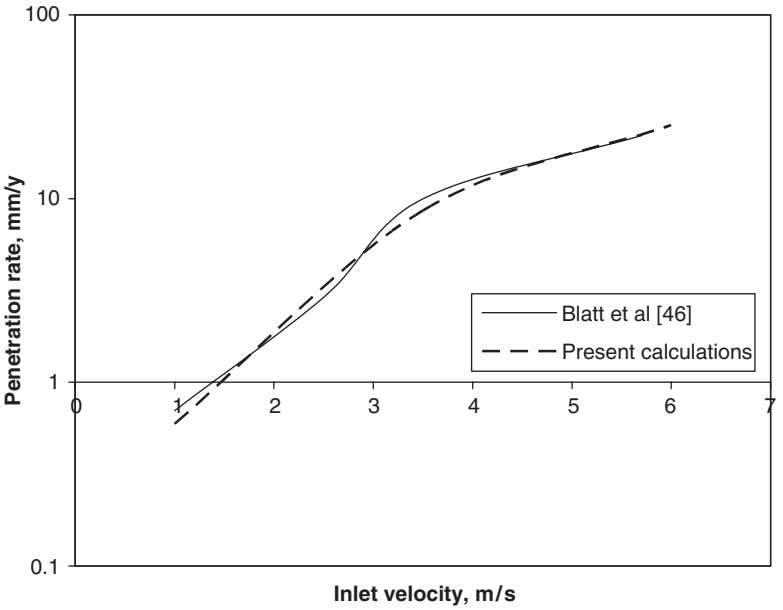

Figure 6. Comparison of the calculated penetration rate and the experimental data of Blatt *et al.* [46].

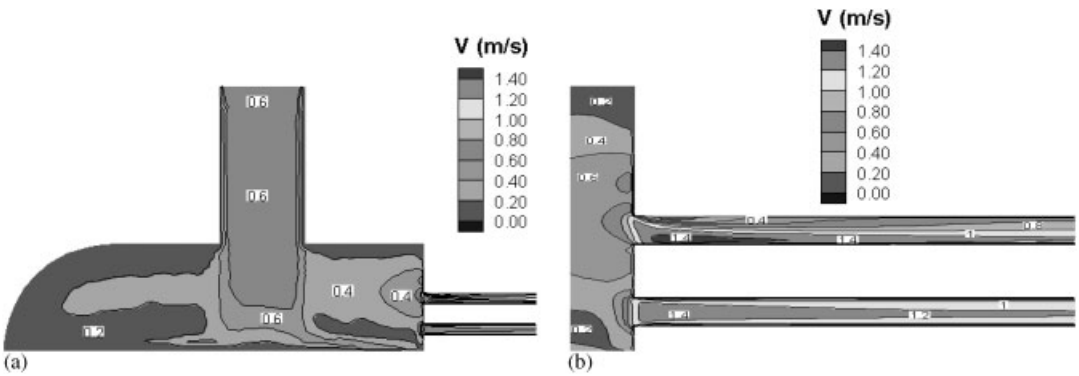

Figure 7. The velocity contours at the plane of symmetry in the header of the shell-and-tube heat exchanger for the case of $V_i = 0.64\,\mathrm{m/s}$: (a) velocity contours at the header plane of symmetry; and (b) velocity contours near the pipe inlet section.

reflects the complexity of the flow pattern that possesses vortical-type motions in different regions of the header. These vortical/swirling motions may be responsible for the high fluid velocity in the vicinity of the tube inlet section.

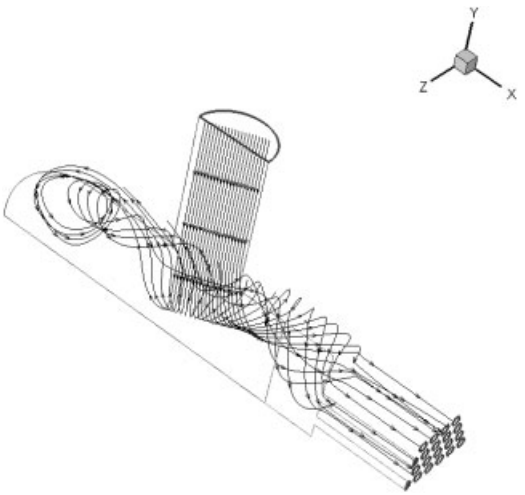

Figure 8. Three-dimensional pathlines for a number of fluid particles in one half of the header of the shell-and-tube heat exchanger for the case of $V_i = 0.64$ m/s.

5.3. The particle tracking results

To determine the rate of erosion using erosion models, the details of particle motion are needed before each impact including particle trajectory, particle velocity and impact angle. In this approach, a large number of sand particles (426 particles of density of 2650 kg/m^3) were first spread uniformly at the header inlet section and then set to move with the water stream inside the header. The number of injected particles is limited by the number of control volumes at the entrance section which is 426 volumes. The initial particle velocity at the time of release was equal to the local flow velocity. Some of these particles made several impacts with various surfaces before entering the heat exchanger tube while a few others dismissed without making a single impact. The trajectory of the particle and its residence time are shown in Figure 9. The residence time is defined as the time taken from the moment a particle is released until it leaves the heat exchanger tubes.

The effect of inlet flow velocity on particle trajectory for a small number of particles is shown in Figures 9(a), (b) and (c) for inlet velocities of 0.3, 1.31 and 2.95 m/s, respectively. In this case, the particle size was kept unchanged ($D_p = 200\,\mu$m) for all three velocities. For the majority of the solid particles, the particle residence time decreases with the increase of the flow velocity at the header inlet. At high velocity, the particle gain more momentum and their velocity increase, thus the residence time decreases. The calculations have also shown that a larger number of impacts occur as the velocity at the header inlet gets higher. This is expected because of the increase of the vortical-type fluid motion in the header. Such increase creates more changes in the direction of fluid motion that results in more solid particles impacting the surface. As well, for low velocity, the large diameter particles tend to reside at the base of the header. As the velocity increases, this is significantly reduced and cause particles to move and cause more impacts at the tube sheet.

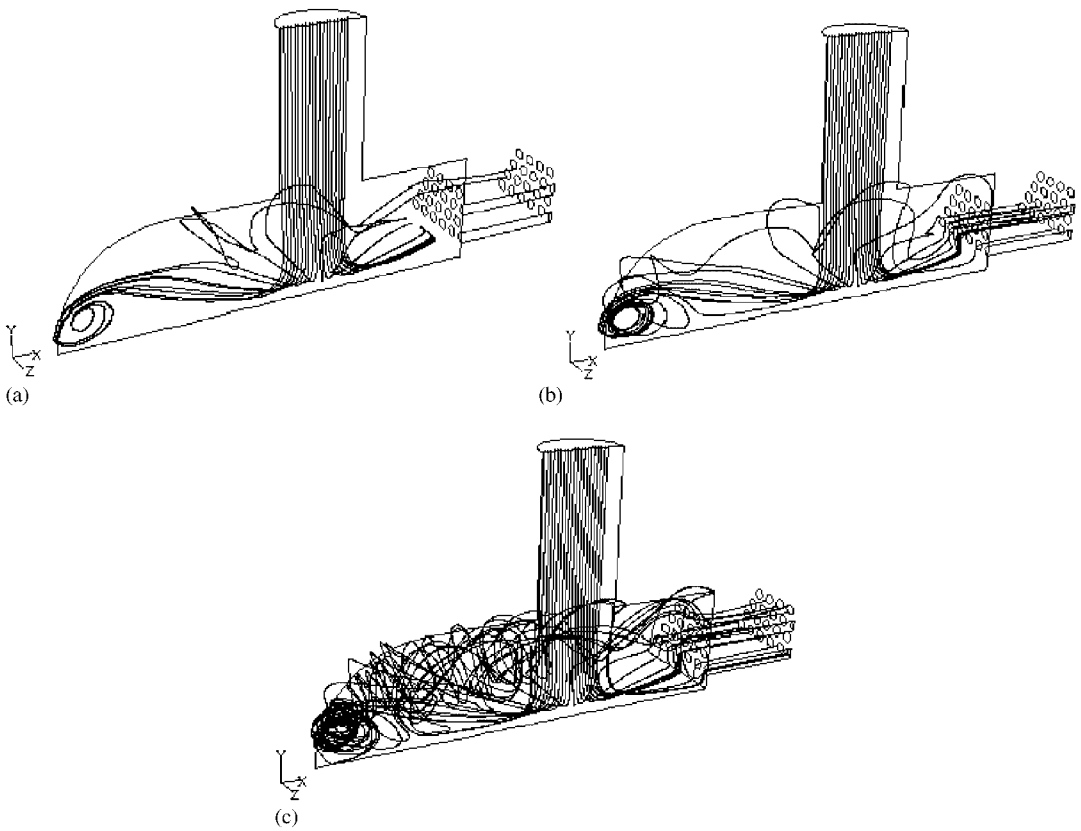

Figure 9. The effect of inlet velocity on the trajectories of a number of sand particles released at the same time at the inlet section of the shell-and-tube heat exchanger header for the case of $D_p = 200\,\mu m$: (a) inlet velocity $V_i = 0.3$ m/s; (b) inlet velocity $V_i = 1.31$ m/s; and (c) inlet velocity $V_i = 2.95$ m/s.

5.4. Erosion rates

As presented earlier in Figures 1 and 2, the inlet header has a semi-circular section with a tube sheet containing a total of 38 tubes arranged in four rows. The number of tubes in each of the four rows (from the lowest row up) is 11, 10, 9 and 8, respectively. Because of symmetry about plane *A–A*, the erosion rates will be determined in one half of the flow domain. Figure 10 shows the erosion rate (in milligram per gram of solid particles) in each tube inlet region for the four rows considering particles of diameter $D_p = 200\,\mu m$ and inlet velocities of 1.31 and 2.95 m/s. Negligible erosion in all tubes was indicated for inlet flow velocities up to 0.64 m/s and, therefore, are not presented in Figure 10. The erosion rates at inlet to the tubes became appreciable when the inlet velocity increased to 1.31 m/s. In this case, the tube suffering maximum erosion is tube #5 in the third row as shown in Figure 10(a) where the erosion rate reached 2.78×10^{-8} mg/g. For the high inlet velocity of $V_i = 2.95$ m/s, the erosion rates became considerable as shown in Figure 10(b). The highest erosion rates are

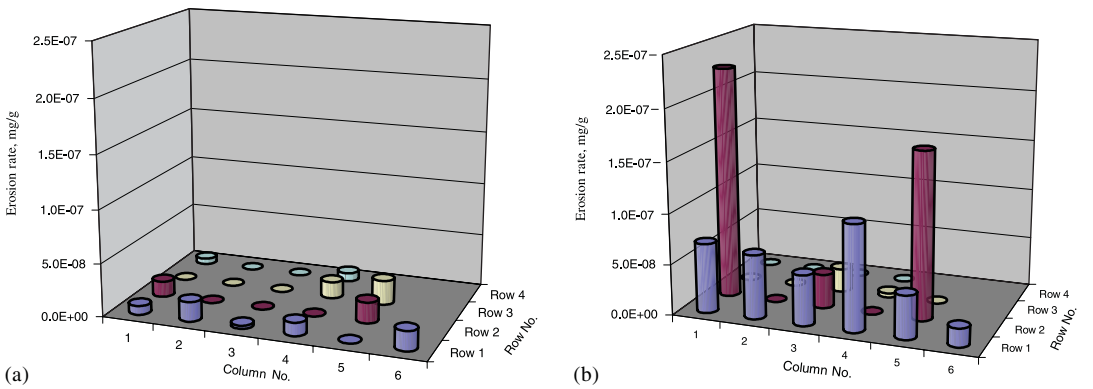

Figure 10. The effect of the inlet velocity, V_i, on the erosion rate in the tubes of the shell-and-tube heat exchanger for the case of $D_p = 200\,\mu m$: (a) $V_i = 1.31$ m/s; and (b) $V_i = 2.95$ m/s.

found to occur in tubes #1 and 5 of the second row (tube #1 is the tube in the second row near the plane of symmetry *A–A* shown in Figure 2). These erosion rates reached 2.4×10^{-7} mg/g in tube #1 and 1.9×10^{-7} mg/g in tube #5. The other tubes experiencing moderate erosion are those #1, 2, 3, 4 and 5 in the first row where the erosion rates range from 5×10^{-8} to 1.25×10^{-7} mg/g. The increase in erosion rate with inlet velocity is mainly due to the increase in the number of impacts as well as the impact velocities caused by the change in the flow structure as manifested by the trajectories shown in Figure 9. The figure also shows that most of the particles impingements occur on the first and second rows. This explains the high rate of erosion in these two rows.

The effect of inlet flow velocity on the total erosion rate (erosion rate summed up for all tubes) is shown in Figure 11 for the three particle sizes ($D_p = 10$, 200 and 350 μm). At the very low velocity of 0.197 m/s, the total erosion rate for the large particle size ($D_p = 350\,\mu m$) is insignificant (does not appear in the figure because of its very small value). On the other hand, the small particles ($D_p = 10\,\mu m$) cause more erosion than the moderate size particles of diameter 200 μm at this velocity. This trend can be explained based on the fact that large particles settle down on the base plate of the inlet header when the flow velocity is small. This occurs mainly because gravity forces outweigh the hydrodynamic forces acting on the particle at low flow velocities. Accordingly, very few particle impingements occur at the tube inlet region in the cases of moderate and large particle sizes. At the moderate velocities of 0.64 and 1.31 m/s the total erosion rates are almost the same for all particle sizes as shown in Figure 11. The same trend is noted at the high velocity of 2.95 m/s, however, with larger differences in the total erosion rates. The highest erosion rate (8.0×10^{-7} mg/g) is caused by the moderate size particles while the lowest rate (4.4×10^{-7} mg/g) is caused by the large size particles.

The total erosion rate occurring in the line (row) of maximum erosion (erosion rate summed up for all tubes in the row of maximum erosion) is shown in Figure 12 for different inlet flow velocities and different particle sizes. The increase of the total erosion rate is quite expected because of the increase in the particle impact velocity as the inlet flow velocity increases. The dependence of erosion rate on particle impact velocity is clear in Equations (14) and (15).

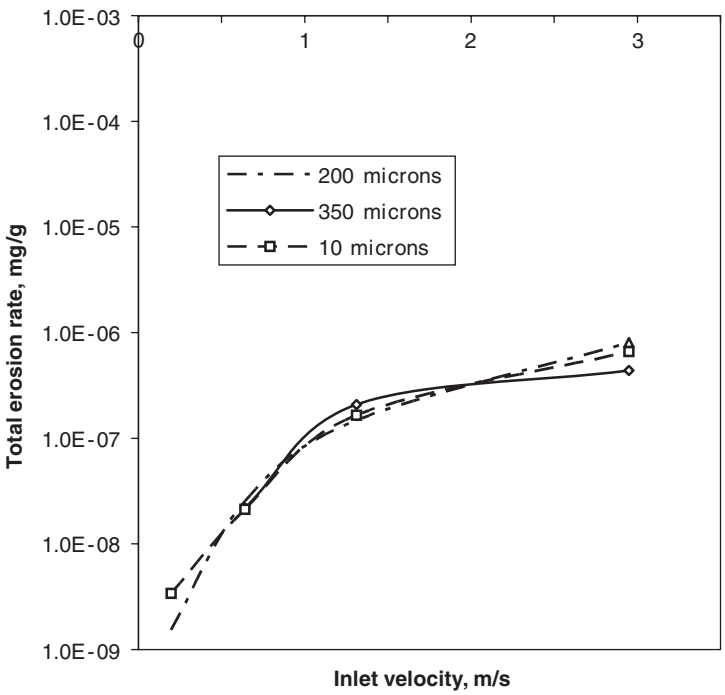

Figure 11. Effect of inlet flow velocity on the total erosion rate for the three particle sizes, $D_p = 10, 200,$ and 350 μm.

The figure also shows the same maximum line erosion rate for all particle sizes at low flow velocities (up to 1.31 m/s). The resulting maximum line erosion rate is almost the same for all particle sizes with some differences at the high velocity of 2.95 m/s. The effect of flow velocity and particle size on erosion in the most critical tube (tube of maximum erosion) is shown in Figure 13. The figure clearly shows the continuous increase in the erosion rate with the increase of the flow velocity for all particle sizes. At low velocities, erosion in the most critical tube is insignificant for all particle sizes (does not exceed 10^{-9} mg/g) and the highest erosion is caused by small particles ($D_p = 10$ μm). This can be explained based on the fact that small particles follow the motion of the fluid stream at low flow velocity because of their insignificant buoyancy forces. In this case, the impact velocity of small particles is of the same order of magnitude of the flow velocity. However, for large particles, the buoyancy forces are significant at this low velocity and some of these particles will settle on the base plate, thus causing less number of impacts in the tube entrance region. This was indicated by the number of particles escaping through the tubes where this number decreased as the particle size increased. As the velocity increases, the significance of the buoyancy of the large size particles decreases and higher erosion rates occur. This is shown in the figure where, in the range of moderate velocities (0.64 and 1.31 m/s), the highest erosion rate in the most critical tube is caused by the large size particles ($D_p = 350$ μm). However, at the high flow velocity of 2.95 m/s, the highest erosion rate (2.28×10^{-7} mg/g) is caused by the moderate

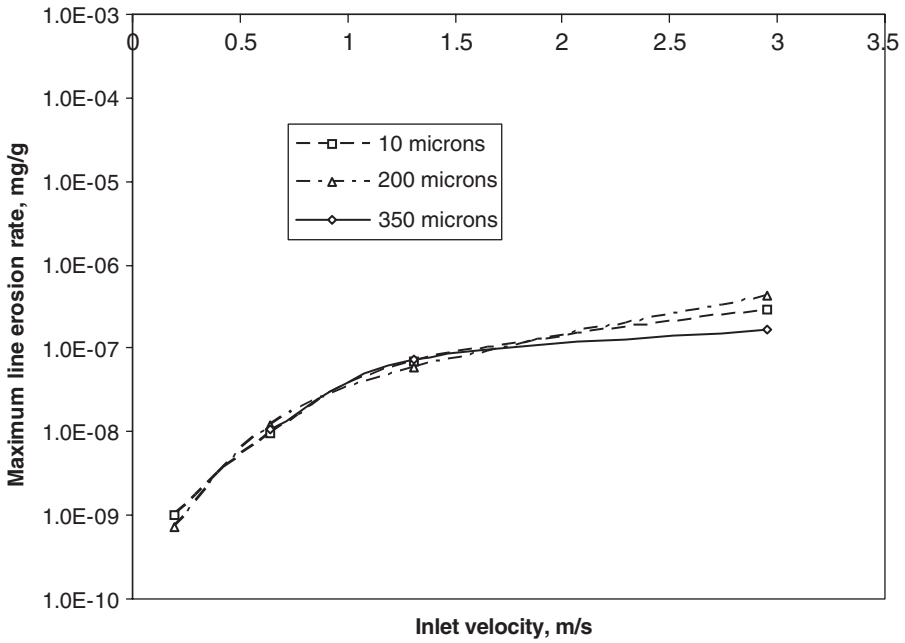

Figure 12. Variation of the total erosion rate in the line of maximum erosion with inlet flow velocity for the three particle sizes.

size particles ($D_p = 200\,\mu m$) and the lowest erosion rate (7.81×10^{-8} mg/g) is caused by the large size particles ($D_p = 350\,\mu m$). It should be emphasized here that the effect of particle size on the erosion pattern and erosion rate is governed by many factors. For example, the amount of erosion caused by unit mass of particles depends on the erosion caused by each impact as well as the number of impacts. As the particle size increases the number of particles (per unit mass) gets less causing less number of impacts. In addition, the particle size has a direct effect on the particle trajectory, point of impact, velocity of impact and angle of impact. In particular, for the tube of maximum erosion, Figure 12, the erosion rate is significantly influenced by the type of trajectory of particles that, in turn, influences the number of impacts on a certain tube. The trajectory depends on the particle size and flow velocity. All these factors have considerable effect on the erosion pattern and erosion rate.

To show the effect of particle size on the erosion characteristics in the inlet region of the heat exchanger tubes, Figure 14 is plotted with its abscissa representing the particle diameter and its ordinate representing the total erosion rate, the maximum line erosion rate (erosion rate summed up for all tubes in the row of maximum erosion) and the maximum tube erosion rate. The results shown in the figure are obtained for the typical inlet flow velocity of 0.64 m/s. At this velocity, the highest total erosion rate reached a value of 5.3×10^{-8} mg/g and occurred when using sand particles of diameter $D_p = 100\,\mu m$. Smaller and larger particles caused less erosion. The trend is very much the same for both maximum line erosion rate and maximum tube erosion rate where the highest value occurred at the same particle diameter. The maximum

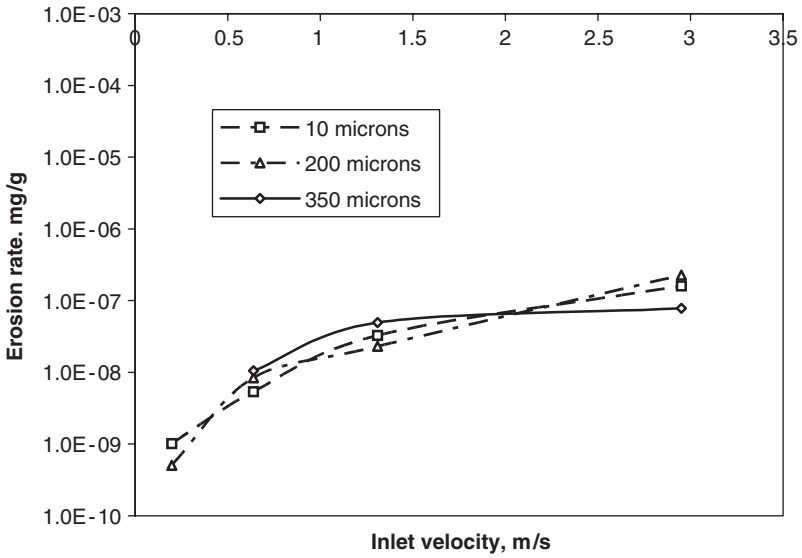

Figure 13. Variation of erosion rate in the most critical tube (tube of maximum erosion) with inlet flow velocity for the three particle sizes.

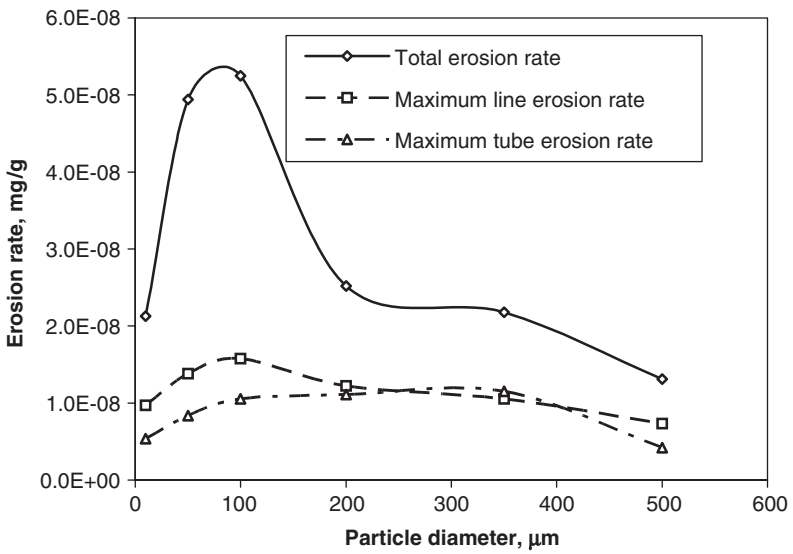

Figure 14. Effect of particle size on the total erosion rate, the maximum line erosion rate and the maximum tube erosion rate in case of $V_i = 0.64$ m/s.

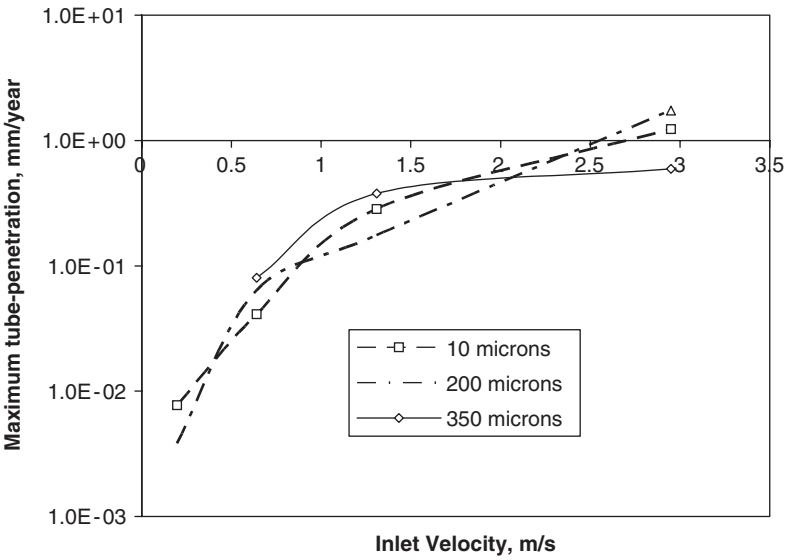

Figure 15. Influence of inlet-header velocity on maximum tube-penetration.

line erosion rate reached about 1.5×10^{-8} mg/g while the maximum tube erosion rate reached 10^{-8} mg/g. The results for particle trajectory show that the number of particles having impact on the tube sheet decreases as the particle size increases. This explains the general decay (apart from size $D_p = 10\,\mu m$) of erosion rate shown in Figure 14 as the particle size increases.

5.5. *Penetration rates*

The local penetration rate represents the depth of wear due to metal removal caused by the erosion process. Figure 15 shows the maximum tube penetration rate and its variation with inlet flow velocity and particle size for the shell-and-tube heat exchanger. The calculations were carried out for the same four values of the inlet flow velocity (0.197, 0.64, 1.31 and 2.95 m/s) and also the same three particle sizes ($D_p = 10$, 200 and 350 μm). In all calculations, the sand flow rate was taken as 5.66×10^{-3} m^3/day that corresponds to 0.0003% sand concentration (by volume) for the case of typical velocity value of 0.64 m/s. The figure shows a very small penetration rate ($P_n < 0.01$ mm/year) for all particle sizes at the low flow velocity of 0.197 m/s. At the typical inlet flow velocity of 0.64 m/s, the maximum tube penetration rate ranges between 0.04 and 0.08 mm/year. When the flow velocity increased to 1.31 m/s, the maximum tube penetration rate reached its highest value of 0.378 mm/year for the large size particles (350 μm) and found to be much less for the other two sizes (about 0.28 mm/year for the 10 μm particles and 0.18 mm/year for the 200 μm particles). At the highest flow velocity of 2.95 m/s, the maximum penetration rate was caused by moderate size particles (1.73 mm/year) while that for large particles increased to about 0.6 mm/year. The maximum tube penetration rate caused by small particles was increased to 1.23 mm/year at this high flow velocity. The dependence of penetration rate on flow velocity is obvious since higher impacting velocity

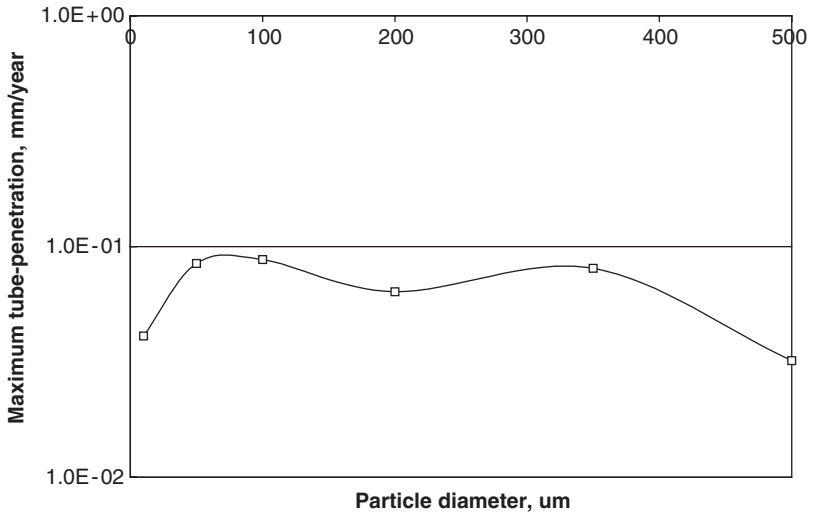

Figure 16. Influence of particle size on maximum tube-penetration for inlet velocity of 0.64 m/s.

causes more erosion and more penetration. However, the effect of particle size on the rate of penetration is influenced by many factors as explained in Section 5.4.

At the typical inlet flow velocity of 0.64 m/s, the effect of particle size on the maximum tube penetration rate, $(P_n)_{\max}$, was investigated considering six different particle sizes ($D_p = 10, 50, 100, 200, 350$ and $500\ \mu m$). The variation of $(P_n)_{\max}$ with particle diameter is shown in Figure 16. The values of $(P_n)_{\max}$ ranged from 0.04 to 0.088 mm/year with the minimum occurring for particles of diameter 500 μm. Particle sizes between 50 and 350 μm created maximum penetration rates ranging between 0.064 and 0.088 mm/year as shown in Figure 16. The occurrence of minimum erosion when using heavy particles at the low velocity of 0.64 m/s is quite expected due to the large contribution of the gravitational force that causes a good percentage of the solid particles to reside on the base plate of the inlet header.

6. CONCLUDING REMARKS

The effects of fluid flow velocity and sand particle size on the rate of erosion in shell-and-tube heat exchangers have been investigated using the Lagrangian particle tracking method. A flow visualization experiment was conducted with the objective of verifying the accuracy of the continuous phase model. The comparison between the visualized flow patterns and the computed velocity vectors resulted in a reasonably good agreement. The erosion results were validated by comparing the calculated penetration rates with available data of flow in pipes with sudden contraction.

The erosion behaviour in the shell-and-tube heat exchanger was predicted for flow velocities in the range 0.197–2.95 m/s considering sand particles of diameters ranging from 10 to 500 μm. The erosion rate was found to increase with the increase of the inlet flow ve-

locity for all particle sizes. Erosion in the most critical tube is insignificant (did not exceed 10^{-9} mg/g) at the low velocity of 0.197 m/s and the highest erosion was caused by small particles ($D_p = 10\,\mu m$). In the range of moderate velocities (0.64 and 1.31 m/s), the highest erosion rate in the most critical tube was caused by the large size particles and was slightly less for the other two particle sizes. For the high velocity of 2.95 m/s, the highest tube erosion was caused by moderate size particles ($D_p = 200\,\mu m$) and was slightly less for the small size particles ($D_p = 10\,\mu m$). For the typical inlet flow velocity of 0.64 m/s, the highest total erosion rate reached a value of 5.3×10^{-8} mg/g.

The maximum tube penetration rate for the shell-and-tube heat exchanger was calculated for all particles sizes in the same flow velocity range assuming a constant sand rate of 5.66×10^{-3} m^3/day. At the low flow velocity of 0.197 m/s, the penetration rate was very small (less than 0.01 mm/year) for all particle sizes. At the typical inlet velocity of 0.64 m/s, the maximum tube penetration rate ranged between 0.06 and 0.09 mm/year with the highest occurring for particles of diameters between 50 and 350 μm. When the flow velocity increased to 1.31 m/s, the maximum tube penetration rate reached its highest value of 0.378 mm/year for the large size particles (350 μm) and found to be much less for the other two sizes (about 0.28 mm/year for the 10 μm particles and 0.18 mm/year for the 200 μm particles). At the high flow velocity of 2.95 m/s, the maximum penetration rate was caused by moderate size particles (1.73 mm/year) while that for large particles increased to about 0.6 mm/year.

NOMENCLATURE

A impingement area defined in Equation (16)
b constant defined in Equation (11)
C_D drag coefficient
C_μ constant defined in Equation (4)
$C_{\varepsilon 1}$ constant defined in Equation (6)
$C_{\varepsilon 3}$ constant defined in Equation (8)
D diameter of the large tube of the sudden contraction simulating Postlethwaite and Nesic [33]
D_p solid particle diameter
d diameter of the small tube of the sudden contraction simulating Postlethwaite and Nesic [33]
E the rate of erosion (mg/g)
E_{lc} local rate of erosion (mg/g)
F force
G_k generation of turbulent kinetic energy
g gravitational acceleration
k turbulent kinetic energy
m_p mass of individual particle
N_p total number of particles being tracked defined in Equation (14)
p pressure
P_n penetration rate defined in Equation (16)
Re_p particle Reynolds number
s surface area

$\dot{s}$ sand rate defined in Equation (16)
$\bar{U}_j$ average velocity component
$\underline{u}$ fluid velocity vector
u_j fluctuating velocity component
u_p particle velocity
V_i flow velocity at the header inlet nozzle
V_{mag} magnitude of velocity (m/s)
x_j space coordinate
t time

Greek letters

α the impact angle
γ the cutting wear coefficient
ε dissipation rate of turbulent kinetic energy
μ dynamic viscosity
ρ density
ρ_m density of target material
σ the deformation wear coefficient
σ_k effective Prandtl number for k
σ_ε effective Prandtl number for ε

Superscript

— time average

Subscripts

D drag
f fluid
sl Saffman lift
p particle
pg pressure gradient
vm virtual mass

ACKNOWLEDGEMENTS

The authors wish to acknowledge the support received from King Fahd University of Petroleum and Minerals during the course of the study. The support received from Saudi Aramco for this research work is also acknowledged.

REFERENCES

1. Rochester MC, Brunton JH. Influences of physical properties of the liquid on the erosion of solids. *Erosion, Wear and Interfaces with Corrosion ASTM STP 567*, American Society of Testing and Materials, 1974; 128–151.
2. True ME, Weiner PD. A laboratory evaluation of sand erosion of oil and gas well production equipment. *Annual API Production Division Meeting*, Los Angeles, CA, 1976; I-1, I-27.

3. Glaeser WA, Dow A. Mechanisms of erosion in slurry pipelines. *Proceedings of the Second International Conference on Slurry Transportation*, Las Vegas, NV, 2–4 March, 1977; 136–140.
4. Roco MC, Nair P, Addie GR, Dennis J. Erosion of concentrated slurries in turbulent flow. *Journal of Pipelines* 1984; **4**:213–221.
5. Venkatesh ES. Erosion damage in oil and gas wells. *Rocky Mountain Regional Meeting of the Society of Petroleum Engineers*, *SPE Paper 15183*, Billings, MT, 1986.
6. Shook CA, Mckibben M, Small M. Experimental investigation of some hydrodynamics factors affecting slurry pipeline wall erosion. *ASME Paper No. 87-PVP-9*, 1987.
7. Chen XH, McLaury BS, Shirazi SA. Application and experimental validation of a computational fluid dynamics (CFD)-based erosion prediction model in elbows and plugged tees. *Computers and Fluids* 2004; **33**(10): 1251–1272.
8. McLaury BS, Wang J, Shirazi SA, Shadley JR, Rybicki EF. Solid particle erosion in long radius elbows and straight pipes. *Society of Petroleum Engineers*, *Paper No. SPE 38842*, 1997; 977–986.
9. Edwards JK, McLaury BS, Shirazi SA. Evaluation of alternative pipe bend fittings in erosive service. *Proceedings of 2000 ASME Fluids Engineering Summer Meeting*, *Paper No. FEDSM 2000-11245,* Boston, MA, 11–15 June 2000.
10. Durst F, Milojevic D, Schonung B. Eulerian and Lagrangian predictions of particulate two-phase flows: a numerical study. *Journal of Applied Mathematical Modeling* 1984; **8**:101–115.
11. Boulet P, Oesterle B, Andreux R. Comparisons between Eulerian–Eulerian and Eulerian–Lagrangian formulation of a gas–solid suspension flow in a heated pipe. *Proceedings of the 1999 ASME Fluids Engineering Division Summer Meeting*, San Francisco, CA, *FEDSM99-7860*, 1999.
12. Lee BE, Tu JY, Fletcher CAJ. On numerical modeling of particle-wall impaction in relation to erosion prediction: Eulerian versus Lagrangian method. *Wear* 2002; **252**:179–188.
13. Wallace MS, Peters JS, Scanlon TJ, Dempster WM, McCulloch S, Ogilvie JB. CFD-based erosion modeling of multi-orifice choke valves. *Proceedings of 2000 ASME Fluids Engineering Summer Meeting*, *Paper No. FEDSM 2000-11244*, Boston, MA, 11–15 June 2000.
14. Graham DI. An improved eddy interaction model for numerical simulation of turbulent particle dispersion. *ASME Journal of Fluids Engineering* 1996; **118**:819–823.
15. Wang J, Shirazi SA, Shadley JR, Rybicki EF. *Application of Flow Modeling and Particle Tracking to Predict Sand Erosion Rates in 90-degree Elbows*, vol. FED-236. *1996 ASME Fluids Engineering Division Conference*, vol. 1, 1996; 725–734.
16. Ahlert KR. Effects of particle impingement angle and surface wetting on solid particle erosion on ANSI 1018 steel. *M.S. Thesis*, University of Tulsa, U.S.A., 1994.
17. Shirazi SA, Shadley JR, McLaury BS, Rybicki EF. A procedure to predict solid particle erosion in elbows and tees. *Journal of Pressure Vessel Technology* 1995; **117**:45–52.
18. Shirazi SA, McClaury BS, Shadley JR, Rybicki EF. Generalization of the API RP 14E guideline for erosive services. *Journal of Petroleum Technology* (*Distinguished Author series*) 1995; **47**(8):693–698.
19. Keating A, Nesic S. Particle tracking and erosion prediction in three-dimensional bends. *Proceedings of 2000 ASME Fluids Engineering Summer Meeting*, *Paper No. FEDSM 2000-11249*, Boston, MA, 11–15 June 2000.
20. Hanson R, Patel MK. Development of a model to predict the life of pneumatic conveyor bends subject to erosive wear. *Proceedings of 2000 ASME Fluids Engineering Summer Meeting*, *Paper No. FEDSM 2000-11246*, Boston, MA, 11–15 June 2000.
21. Forder A, Thew M, Harrison D. A numerical investigation of solid particle erosion experienced within oilfield control valves. *Wear* 1998; **216**:184–193.
22. Tilly GP. Erosion caused by impact of solid particles. In *Treatise on Materials Science and Technology*, Preece CM (ed.), vol. 13. Academic Press: New York, 1979.
23. Ruff AW, Wiederhorn SM. Erosion by solid particle impact. In *Treatise on Materials Science and Technology*, Preece CM, vol. 16. Academic Press: New York, 1979; 69–125.
24. Davies JE, Stead RJ, Andrews CJ, Richards JR. The airborne particle erosion resistance of a range of engineering materials. *Key Engineering Materials* 1991; **117**:45–52.
25. Habib MA, Attya AE, McEligot DM. Calculation of turbulent flow and heat transfer in channels with streamwise periodic flow. *ASME Journal of Turbomachinery* 1989; **110**:405–411.
26. Versteeg HK, Malalasekera W. *An Introduction to Computational Fluid Dynamics*; *The Finite Volume Method.* Longman Scientific and Technical: New York, 1995.
27. Choudhury D. Introduction to the renormalization group method and turbulence modeling. *Fluent Inc.*, *Technical Memorandum TM-107*, 1993.
28. Reynolds WC. *Fundamentals of Turbulence for Turbulence Modeling and Simulation*. Lecture Notes for Von Karman Institute. *Agard Report No. 755*, 1987.
29. Shih TH, Liou WW, Shabbir A, Zhu J. A new k–ε eddy-viscosity model for high Reynolds number turbulent flows—model development and validation. *Computers and Fluids* 1995; **24**(3):227–238.
30. Launder BE, Spalding DB. The numerical computation of turbulent flows. *Computer Methods in Applied Mechanics and Engineering* 1974; **3**:269–289.

31. Benchaita MT, Griffith P, Rabinowicz E. Erosion of metallic plate by solid particles entrained in a liquid jet. *Journal of Engineering for Industry* 1983; **105**:215–222.
32. Lu QQ, Fontaine JR, Aubertin G. A Lagrangian model for solid particles in turbulent flows. *International Journal of Multiphase Flow* 1993; **19**(2):347–367.
33. Postlethwaite J, Nesic S. Erosion in disturbed liquid/particle pipe flow, effects of flow geometry and particle surface roughness. *Corrosion* 1991; **49**:850–859.
34. Saffman PG. The lift on a small sphere in a slow shear flow. *Journal of Fluid Mechanics* 1965; **22**(2): 385–400.
35. Morsi SA, Alexander AJ. An investigation of particle trajectories in two-phase flow systems. *Journal of Fluid Mechanics* 1972; **52**(2):193–208.
36. Haider A, Levenspiel O. Drag coefficient and terminal velocity of spherical and nonspherical particles. *Powder Technology* 1989; **58**:63–70.
37. Tabakoff W, Wakeman T. Measured particle rebound characteristics useful for erosion prediction. *ASME Paper 82-GT-170*, 1982.
38. Isomoto Y, Nishimura M, Nagahashi K, Matsumura M. Impact angle dependence of erosion by solid particle impact for metallic materials. *Erosion Engineering* 1999; **48**(6):355–361.
39. McLaury BS, Shirazi SA. Predicting erosion in straight pipes. *Proceedings of the 1998 ASME Fluids Engineering Division*, June 21–25, Washington D.C., *Paper No. FEDSM 98-5226*, 1998.
40. Finnie I. The mechanism of erosion of ductile metals. *Proceedings of 3rd US National Congress of Applied Mechanics*, 1958; 527–532.
41. Finnie I, Stevick GR, Ridgely JR. The influence of impingement angle on the erosion of ductile metals by angular abrasive particles. *Wear* 1992; **152**:91–98.
42. Shirazi SA, McLaury BS. Erosion modeling of elbows in multiphase flow. *Proceedings of 2000 ASME Fluids Engineering Summer Meeting*, 11–15 June 2000, Boston, MA, *Paper No. FEDSM 2000-11251*.
43. Neilson JH, Gilchrist A. Erosion by a stream of solid particles. *Wear* 1968; **11**:111–122.
44. *Fluent 5 User's Guide*. Fluent Inc., 1998.
45. Schlichting H. *Boundary Layer Theory*. McGraw Hill: New York, 1979.
46. Blatt W, Kohley T, Lotz U, Heitz E. The influence of hydrodynamics on erosion-corrosion in two-phase liquid particle flow. *Corrosion* 1989; **45**(10):793–804.
47. Bell KJ, Mueller AC. *Engineering Data Book II*. Wolverine Division of UOP Inc. (One of the Signal Companies), 1984.

